Improving hydrogen release from oxygen-functionalized LOHC molecules by Ru addition to Pt/C catalysts

Lukas A. Maurer[a,b,+], Chuyen Pham[a,+], Birk Fritsch[a], Henrik S. Jeppesen[c], Martin Etter[c], Andreas Hutzler[a], Reinhard Neder[d], Moritz Wolf[e], Franziska Auer[a], Simon Thiele[a,b], Peter Wasserscheid[a,b,f*]

[a] Forschungszentrum Jülich GmbH, Helmholtz Institute Erlangen-Nürnberg for Renewable Energy (IEK-11), Erlangen, Germany

[b] Friedrich-Alexander-Universität Erlangen-Nürnberg (FAU), Institute of Chemical Reaction Engineering (CRT), Erlangen, Germany

[c] Deutsches Elektronensynchrotron DESY, Hamburg, Germany

[d] Friedrich-Alexander-Universität Erlangen-Nürnberg (FAU), Institute for Crystallography and Structural Physics, Erlangen, Germany

[e] Karlsruhe Institute of Technology (KIT), Engler-Bunte-Institut & Institute of Catalysis Research and Technology, Karlsruhe, Germany

[f] Forschungszentrum Jülich GmbH, Institute for a Sustainable Hydrogen Economy, Jülich, Germany

[+] These authors contributed equally to this work.

[*] Corresponding author. Address: Cauerstr. 1, 91058 Erlangen. E-Mail-address: p.wasserscheid@fz-juelich.de

Abstract

Bimetallic PtRu/C catalysts have been prepared by depositing Ru onto a commercial Pt/C catalyst and subsequent thermal annealing. Different Pt:Ru ratios of 1:1, 2:1, 4:1, 8:1, and 16:1 have been investigated with annealing temperatures of 350 and 500 °C. Using X-ray diffraction (XRD), synchrotron powder X-ray diffraction (SPXRD) combined with pair distribution function (PDF) analysis and scanning transmission electron microscopy with energy dispersive X-ray spectrum imaging (STEM-EDXS), we show that diffusion of Ru into the fcc crystal structure of the Pt nanoparticles takes place during thermal annealing. Partial segregation and the formation of Pt nanoclusters on the bimetallic surface was observed depending on the Pt:Ru ratio. The annealing process does not only cause a high Pt dispersion but also affects the electronic structure of the Pt surface by broadening the d-band thus facilitating the product's desorption from the surface of the bimetallic particle. These beneficial effects have been exemplified for the catalytic dehydrogenation of dicyclohexylmethanol, a promising hydrogen carrier compound with 7.2 wt% hydrogen capacity. The most active catalyst material among the tested supported alloys and monometallic reference materials was Pt_4Ru_1/C after annealing at 500 °C, which increased the hydrogen release productivity by 65% compared to the unmodified Pt/C catalyst.

Keywords

Alloys, Chemical hydrogen storage, Dehydrogenation, Heterogeneous catalysis, LOHC, Platinum, Ruthenium.

Introduction

The transport and storage of renewable energy is of great importance in the context of the global energy transition. Liquid organic hydrogen carriers (LOHCs) offer great potential for storing and transporting hydrogen and acting as an infrastructure-compatible energy vector.[1] The most promising and intensively researched LOHC systems consist of aromatic hydrocarbons and their hydrogenated counterparts, e.g. toluene/methylcyclohexane[2,3], (perhydro) dibenzyltoluene (H18-/H0-DBT)[4–7] and (perhydro) benzyltoluene (H12-/H0-BT)[4,7]. Hydrogen is bound covalently to these LOHC molecules, which enables a significant increase in volumetric energy density of hydrogen storage.

The high enthalpy of the dehydrogenation reaction prevents unintended release of hydrogen at ambient conditions, ensuring loss-free storage and safe transport. However, this also means that the catalytic release of hydrogen requires an external energy supply to overcome the reaction enthalpy and maintain the reaction temperature. To keep this effort as low as possible, various strategies for an efficient low-temperature dehydrogenation with a focus on dehydrogenation thermodynamics were discussed by Müller *et al.*[8].

In addition, alternative LOHC systems and more efficient catalysts can reduce dehydrogenation temperatures and thus leverage heat integration potentials, e.g. with the exothermal energetic use of the released hydrogen. LOHC systems, that contain heteroatoms such as nitrogen in (perhydro) N-ethylcarbazole (H12-/H0-NEC), have already been extensively studied and dehydrogenation temperatures below 200 °C have been realized.[9] Nitrogen-containing LOHC systems were found to generally exhibit reduced hydrogenation/dehydrogenation enthalpies.[10]

Recently, also oxygen-containing substances have been evaluated as LOHC compounds. Zakgeym *et al.*[11] showed experimentally that the dehydrogenation of the oxygen-containing dicyclohexylmethanol (H14-BP) to benzophenone (H0-BP) can be conducted at temperatures below 250 °C. Note, that through the introduction of the alcohol functionality the hydrogen capacity rises to 7.2 wt% in comparison to 6.7 wt%[12] for the oxygen-free counterpart (perhydro) diphenylmethane (H12-/H0-DPM).

A promising possibility to reduce dehydrogenation temperatures is the use of a bimetallic catalyst. Bimetallic catalysts often show properties that neither of the two monometallic catalysts exhibit. Depending on the interaction of the two metals, the activity and selectivity of the catalyst can increase. [13]

The geometric and electronic properties of the material can be specifically adjusted [14,15]. This makes it possible to influence the reaction behaviour and the adsorption properties of the catalyst [16,17].

The use of bimetallic platinum ruthenium catalysts was a major breakthrough in electrocatalysis [18,19]. A synergistic effect between platinum and ruthenium leads to unique properties of this catalyst in electrocatalytic applications [20,21].Therefore, these catalysts have been a special focus of research and development in recent years [22]. The activity of such PtRu catalysts can be influenced by various control variables. These include morphological design, adjusting the integration of metal and support and adjusting the electronic structure of the active centres [22].

The introduction of ruthenium leads to a ligand effect and weakens the d-band center of the platinum [23,24]. It has been shown that the use of ruthenium in an alloy with platinum weakens the binding of platinum to adsorbed Co and thus increases the resistance of platinum to poisoning [20,25]. In a further study, a platinum-ruthenium alloy was shown to have significantly increased activity for methanol electrooxidation. This could be attributed to a modification of the electronic structure of the platinum surface through the introduction of ruthenium into the alloy [26].

In this study, we present a bimetallic catalyst, PtRu/C, with improved performance in the thermocatalytic dehydrogenation of H14-BP. We also show the influence of different Ru contents on the performance of the bimetallic catalysts. The addition of the second metal, Ru, to the Pt-based reference catalyst was carried out via an innovative synthesis approach. The results are complemented by a comprehensive catalyst material characterization.

Experimental

Catalyst synthesis

Our innovative synthesis approach was published previously[27] and now scaled up for this study. For the synthesis of the carbon supported Pt_xRu_1 (x = 1, 2, 4, 8, and 16) catalysts (Pt_xRu_1/C), 3 g of Pt/C (5 wt% Pt, Sigma Aldrich) were added to a round bottom flask, followed by addition of 10 ml H_2O to wet the catalyst. Then, 150 ml of isopropanol were added. The Pt/C precursor was dispersed in the solution by sonication for 5 min, followed by stirring for 1 h at 75 °C. A salt precursor solution was prepared by dissolution of a predetermined amount (according to Ru content, x) of hydrated $RuCl_3$ (38-42 wt% Ru, Sigma Aldrich) in 1 ml water by sonication for 2 min. Next, the prepared $RuCl_3$ aqueous solution was added to the reaction

solution under stirring. Deposition of Ru on Pt nanoparticles in the reaction solution occurred under continuous stirring at 600 rpm for 3 h at 75 °C. The reaction solution was then filtered and rinsed with a copious amount of H_2O using a glass vacuum filtration system. The received product was dried in a freeze drier for 6 h. An annealing step was carried out in reductive gas atmosphere (10% H_2 in Ar) at 350 °C or 500 °C for 2 h to obtain Pt_xRu_1/C-350 and Pt_xRu_1/C-500, respectively.

Catalyst Characterization

Transmission electron microscopy

The samples for transmission electron microscopy (TEM) investigations were prepared by dip-coating TEM grids with suspensions of Pt_1Ru_x/C powder in a 1:1 mixture of isopropanol and water, followed by natural drying in air. High-angle annular dark field scanning TEM (HAADF-STEM) and energy dispersive X-ray spectrum imaging (STEM-EDXS) were performed using a Talos F200i (Thermo Fisher Scientific) operated at a primary electron energy of 200 keV. In addition, selected area electron diffraction (SAED) was carried out using an aperture of 10 µm diameter yielding a circular field of view of around 230 nm.
Diffraction patterns have been evaluated using an automated evaluation routine based on Python[28]. At first, the algorithm iteratively determines the exact center of the diffraction pattern obstructed by the beam stopper. Next, an aberration correction is performed by fitting elliptical distortions up to fourth order to the polar transformed data[28,29]. In the end, the aberration-corrected diffraction patterns are azimuthally integrated and peak-fitting allows for separation of background and measurement signal. For crystalline materials, the approach was demonstrated to yield ppm accuracy in changes of the reciprocal lattice vector *q*.

XRD measurement

The diffractograms were recorded with a X'Pert PRO MPD diffractometer from Malvern Panalytical with Cu K_α radiation (λ = 1.542 Å). A diffraction angle range of 10 – 90° was measured with a sampling rate of $0.015° \cdot 100\ s^{-1}$. The Profex software was used for the evaluation of the diffraction data. The parameters of the analysis were kept constant for all synthesized catalysts. To compare macroscopic XRD data to nanoscopic SAED patterns, diffraction angles were translated into the *q*-space by the following correlation:

$$q = \frac{2 \sin\theta}{n \cdot \lambda}$$

with the diffraction order n (for first order diffraction $n = 1$), X-ray wavelength λ, and diffraction angle θ.

X-ray atomic pair distribution function analysis

Synchrotron powder X-ray diffraction (SPXRD) measurements were performed at the Powder Diffraction and Total Scattering Beamline P02.1 at the PETRA III synchrotron at the Deutsches Elektronen-Synchrotron at a wavelength of $\lambda = 0.20731$ Å. Samples were put in glass capillaries of 0.8 mm diameter and capillaries were spun during the experiment for better statistics. Each sample was measured for 30 min ensuring high quality data also at high magnitude of scattering values Q. Diffraction data was collected on a Varex XRD 4343CT area detector which has a CsI scintillator directly deposited on amorphous Si photodiodes. The pixel size of the detector is $150 \cdot 150$ µm² and it has a pixel area of $2880 \cdot 2880$ pixels. The detector was placed at a calibrated distance of 300.859 mm from the sample. Dark images with electronic noise of the detector, activated pixels or stray photons from the front part of the beamline before the fast shutter were automatically subtracted from the raw data. A LaB_6 powder standard (NIST 660c) was utilized for the calibration of the detector. Azimuthal integration was performed using the DAWN Science software.[30]

The integrated intensities were converted to the powder pair-distribution-function (PDF) using the ad-hoc algorithm as build into PDFgetx3[31,32]. Our own software DISCUS[33] was used for the data conversion. Comparisons to PDF data converted by PDFgetx3 did not show significant differences in the distance range 1.0 Å to 20 Å. The scattering by the capillary was subtracted using an equivalent data set for an empty capillary. To minimize the effects of the finite Q range, the data were limited to $Q_{max} = 18.0$ Å^{-1}. Following the standard data treatment for the powder PDF, the small angle range below $Q_{min} = 1.15$ Å^{-1} was replaced in the reduced normalized scattering function F(Q) by a straight line to the origin.

Inductively coupled plasma optical emission spectroscopy

To demonstrate the successful deposition of Ru on the commercial Pt/C catalyst during the synthesis, the metal loading of a Pt_1Ru_1/C catalyst with the highest Ru content under

investigation was measured using inductively coupled plasma optical emission spectroscopy (ICP-OES). 100 mg of the catalyst was dissolved with inverse aqua regia (HNO_3:HCl = 3:1). The measurement was carried out with an Agilent 725 device (radial measurement; plasma excitation at 40 MHz, 2 kW) and repeated twice.

Dehydrogenation experiments

The dehydrogenation experiments were carried out in a semi-batch glass setup. The reaction took place in a 100 mL three-neck glass flask, equipped with a reflux condenser and a heating mantle. The temperature of the liquid phase was measured with a type K thermocouple, which was inserted into the liquid through a septum and controlled by a fitron 4 TP temperature controller (Fiege electronic). Customized software (fitronTP V1.0.2b) is used to operate the temperature controller. A continuous flow of 200 ml/min Ar was directed through the entire reaction chamber as carrier gas for the released hydrogen. The argon flow was adjusted with an EL-FLOW Prestige mass flow controller (Bronkhorst), using the Flow View V1.23 software (Bronkhorst). This leads to a shift in the reaction equilibrium and thus favors dehydrogenation. The off-gas from the reaction was passed through the reflux condenser and two washing bottles to remove remaining organic residues. Other gaseous impurities, such as CO_2, were removed with an activated carbon filter. The hydrogen content in the gas stream was measured by means of thermal conductivity measurement (FTC 300; Messkonzept; calibrated range 0 - 40 vol.% H_2 in Ar).

Before the start of the experiment, the hydrogen-loaded LOHC was weighed into the three-neck flask. H14-BP was produced through hydrogenation of benzophenone. Table S3 of the ESI shows the sample composition, and its purity was determined to be 98.42% using GC-FID. The mass of H14-BP amounted to 29.75 g for all experiments (equivalent to 0.15 mol). The amount of catalyst was defined by a fixed molar ratio of LOHC to precious metal (Pt + Ru) of 2000:1. The catalyst was filled into a custom-made stainless-steel sleeve, which was placed in a glass tube connected to the flask. This allowed the release of the catalyst at the desired reaction temperature without opening the system. The LOHC was magnetically stirred at 500 rpm and heated to reaction temperature under argon flow.

When the LOHC reached the desired temperature, a zero sample was taken, the experimental time started, and the catalyst was added. Further samples of 0.1 ml were taken after 30, 60, 90, 120, 180, 240, and 300 min with a 1 ml plastic syringe and a suitable cannula through the flask

side-neck sealed with a septum. The liquid samples were cleaned from residual catalyst particles by a syringe filter and prepared for analysis by gas chromatography (GC). At the end of the experiment, the heating mantle was switched off. As soon as the temperature in the reaction chamber decreased below 50 °C, the cooling, the inert gas supply, and the stirrer were switched off and the experimental setup was disassembled and cleaned.

Regarding the reaction mechanism of H14-BP dehydrogenation, it must be pointed out that hydrogen is released in two stages. First, the alcohol functionality is dehydrogenated resulting in ketone formation. This process accounts for 1/7 of the theoretically possible hydrogen release. Second, the more demanding ring dehydrogenation occurs in the presence of a suitable catalyst. A detailed description of the reaction mechanism was recently published by Zakgeym *et al.*[11].

Gas chromatographic analysis of liquid samples

The composition of the liquid samples from the dehydrogenation experiments was analyzed using GC. For sample preparation, defined amounts of liquid and n-decane standard were weighed into a GC vial, followed by addition of the solvent acetone and homogenization through shaking. The samples were then measured using a Trace 1310 gas chromatograph (Thermo Fisher) with an iConnect™ flame ionization detector (Thermo Fisher). A SRxi17Sil capillary column (Restek, 30 m, inner diameter 0.25 mm) was used for separation. Helium was used as carrier gas with a flow rate of 1 ml/min and a split ratio of 150:1. A sample volume of 1 ml was injected at an injector temperature of 250 °C. Table 1 shows the temperature program, which was optimized for the separation of all occurring products.

Table 1: Temperature program of the GC method for analysis of the liquid phase composition.

Heating ramp / °C min^{-1}	Target temperature / °C	Holding time / min
Start	110	5
10	130	5
5	145	10
5	180	0
10	270	5

Between different measurement sequences, the capillary column was cleaned by injecting acetone onto the column and heating the oven to 300 °C. The chromatograms were generated using the software Thermo Xcalibur Qual Browser.

In our previous work[11] the retention times and the correction factors $K_{i/St}$ of all reaction (side) products and intermediates were determined. The corresponding molar quantities n_i were calculated from the measured peak areas A and molar masses M of all substances i and the standard St using equation 1.

$$n_i = \frac{n_{St} \cdot A_i \cdot M_{St}}{M_i \cdot A_{St}} \cdot K_{i/St} \tag{1}$$

Equation 2 enables the direct calculation of the corresponding molar fractions $\frac{n_i}{n_{tot}}$ in the reaction mixture.

$$\frac{n_i}{n_{tot}} = \frac{\frac{A_i}{M_i} K_{i/st}}{\sum_j \frac{A_j}{M_j} K_{i/st}} \tag{2}$$

The overall proportion of released hydrogen is calculated via the following correlation:

$$\frac{n_{H_2-released}}{n_{H_2-stored}} = \frac{0}{7} \cdot \frac{n_{H14-BP}}{n_{tot}} + \frac{1}{7} \cdot \frac{n_{H12-BP}}{n_{tot}} + \frac{3}{7} \cdot \frac{n_{H8-BP}}{n_{tot}} + \frac{4}{7} \cdot \frac{n_{H6-BP}}{n_{tot}} + \frac{6}{7} \cdot \frac{n_{H2-BP}}{n_{tot}} + \frac{7}{7} \cdot \frac{n_{H0-BP}}{n_{tot}} - \frac{1}{7} \cdot \frac{n_{H12-DPM}}{n_{tot}} + \frac{2}{7} \cdot \frac{n_{H6-DPM}}{n_{tot}} + \frac{5}{7} \cdot \frac{n_{H0-DPM}}{n_{tot}} + \frac{8}{7} \cdot \frac{n_{Fluorenone}}{n_{tot}} \tag{3}$$

Thermal conductivity measurement and gas phase analysis

From the thermal conductivity (TCD) measurement, the volumetric flow rate of hydrogen $\dot{V}_{H_2}$ can be calculated with the following formula:

$$\dot{V}_{H_2} = \frac{\varphi_{H_2}}{1 - \varphi_{H_2}} \cdot \dot{V}_{Ar} \tag{4}$$

Here, φ_{H_2} stands for the measured volume fraction of hydrogen in the exhaust gas stream and $\dot{V}_{Ar}$ for the volumetric flow of argon with which the reaction chamber is overflown. The

productivity *P* of the catalyst is then calculated from the volumetric flow rate of hydrogen as follows:

$$P = \frac{\dot{V}_{H_2} \cdot \rho_{H_2}}{m_{cat} \cdot w_{Pt}} \tag{5}$$

The density of hydrogen at 273.15 K ($\rho_{H_2} = 0.0899$ kg/m^3), the catalyst mass m_{cat} and the metal loading w_{Pt} were used for the calculation. The TCD measurement can be falsified by the presence of other gases like water, which can be formed in side reactions like dehydration. Therefore, all data determined from TCD measurements were fitted to the data points determined by GC. For this purpose, a correction function is used, which is determined by a least-square minimization.

Results and discussion

Catalyst synthesis

The synthesis method used in this work is scalable and was realized at gram-scale. The method consists of two main steps as illustrated in Figure 1. In the first step, Ru metal was deposited onto the Pt nanoparticles of a commercial Pt/C catalyst (Pt loading of 5 wt%). The Ru deposition onto the surface of Pt catalyst particles occurred by a Pt catalyzed Ru^{3+} reduction with isopropanol (equation 6, Figure 1). Table S2 in the SI gives an overview of the target loadings of the individual catalysts. The quantities of precursors used and the annealing temperatures for the individual catalysts can be seen in Table S3. As a result, Ru can be observed in the close vicinity of Pt particles (referred to as $Ru_1@Pt_x/C$) in the obtained EDX spectra (Figure 2, first column).

$$2\ RuCl_3 + 3\ CH_3CH(OH)CH_3 \rightarrow 2\ Ru + 3\ CH_3COCH_3 + 6\ HCl \tag{6}$$

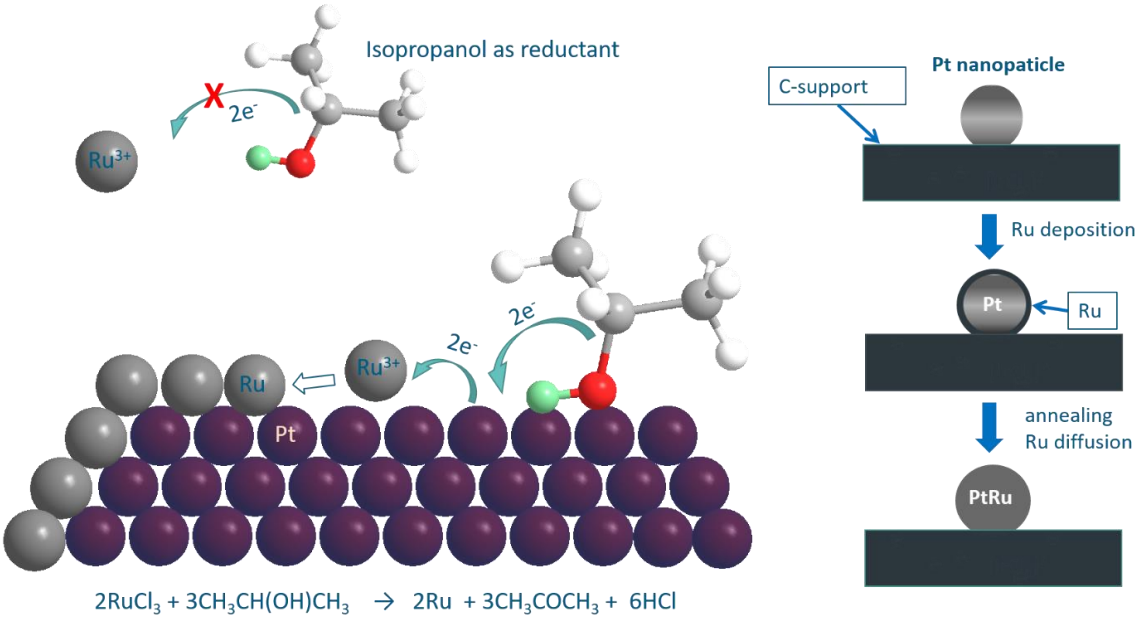

Figure 1: Schematic illustration of the catalyst synthesis process.

To enhance the diffusion of Ru into the Pt lattice, annealing of the $Ru_1@Pt_x/C$ pre-catalyst was carried out under H_2/Ar atmosphere at 350 °C and 500 °C for 2 h to yield Pt_xRu_1/C-350 and Pt_xRu_1/C-500 samples, respectively. The use of a hydrogen atmosphere during the annealing was carried out to ensure that Ru remains in its reduced state during the thermal treatment. The ICP analysis of Pt_1Ru_1/C yield the targeted values with acceptable measurement deviations (see Table S4). The highest utilized ratio of 1:1 was reliably attained, indicating precise control over the synthesis process. It is presumed that all lower Pt:Ru ratios were also successfully achieved, maintaining consistency throughout the experimental procedure. These results underscore the accuracy and reliability of the synthesis method, providing confidence in the subsequent analysis and interpretation of the experimental data.

The annealing step is supposed to enable the diffusion of Ru into Pt particles. Overall, the results of STEM-EDXS measurements suggest that Ru is first deposited onto Pt particles (Figure 2 a), distributes and alloys with Pt upon annealing at 350 °C (Figure 2 b), and partially precipitates again to Ru particles with Pt attached at an annealing temperature of 500 °C (Figure 2 c). The same trend is also observable in Figure S1 and S2 in the supporting information. These results are also confirmed by SAED, as depicted by the radially integrated intensity profile in Figure 3 (corresponding selected areas and diffractograms are shown in Figure S3). Here, diffraction peaks of both Ru and Pt as well as slight peak shifts indicating alloying of both elements are visible, whereas the peaks are remarkably broadened due to the small size of the nanostructures.

Most of the catalyst volume, however, consists of PtRu alloy, which gets obvious when looking at the XRD patterns (Figure 3 and 4). The XRD pattern of $Ru_1@Pt_1/C$ shows diffraction signals at 39.7°, 45.8°, and 67.0° (Figure 4) which are slightly shifted to higher values compared to the values of an ideal Pt crystal at 39.2°, 45.6° and 66.5°[34]. These diffractions correspond to (111), (200) and (220) lattice planes of face-centered cubic Pt (fcc Pt, JCPDS card No.04-802).[35,36] The shifts correlate to the embedding of Ru into Pt lattices.[37–39] Diffraction at 2θ of 25.0° can be assigned to interference at the carbon lattices. No clear separate peaks of Ru metal were observable, indicating an overall alloying of Ru into Pt fcc crystallites[39]. With an increase in the post-treatment temperature, more Ru is incorporated into the Pt crystal, enhancing this shift. This is also visible when comparing Pt_4Ru_1/C-500 and Pt_1Ru_1/C-500 (Figure 4). At the same post-treatment temperature, the sample with more ruthenium shows a larger shift of diffraction peaks. A similar increase in the shift with an increase in the ruthenium content has already been observed by Chu *et al.*[39]. Furthermore, the sharpening of the diffraction peak for Pt_4Ru_1/C-500 indicates a larger spatial coherence and, thus, bigger nanoparticle size compared to Pt/C.[40] From STEM measurements, the diameters of Pt_xRu_1 nanoparticles are estimated in the range of 1 - 6 nm (Figure S4) and well distributed over the carbon micro-particles as shown in Figure 2 and S1. State of the art calculations [41] were used to determine particle size distribution and the metal dispersion (see figure S4 and Table S1 in SI). We observed sintering of the bimetallic nanoparticles for Pt_xRu_1/C-500 samples because of the elevated annealing temperature.

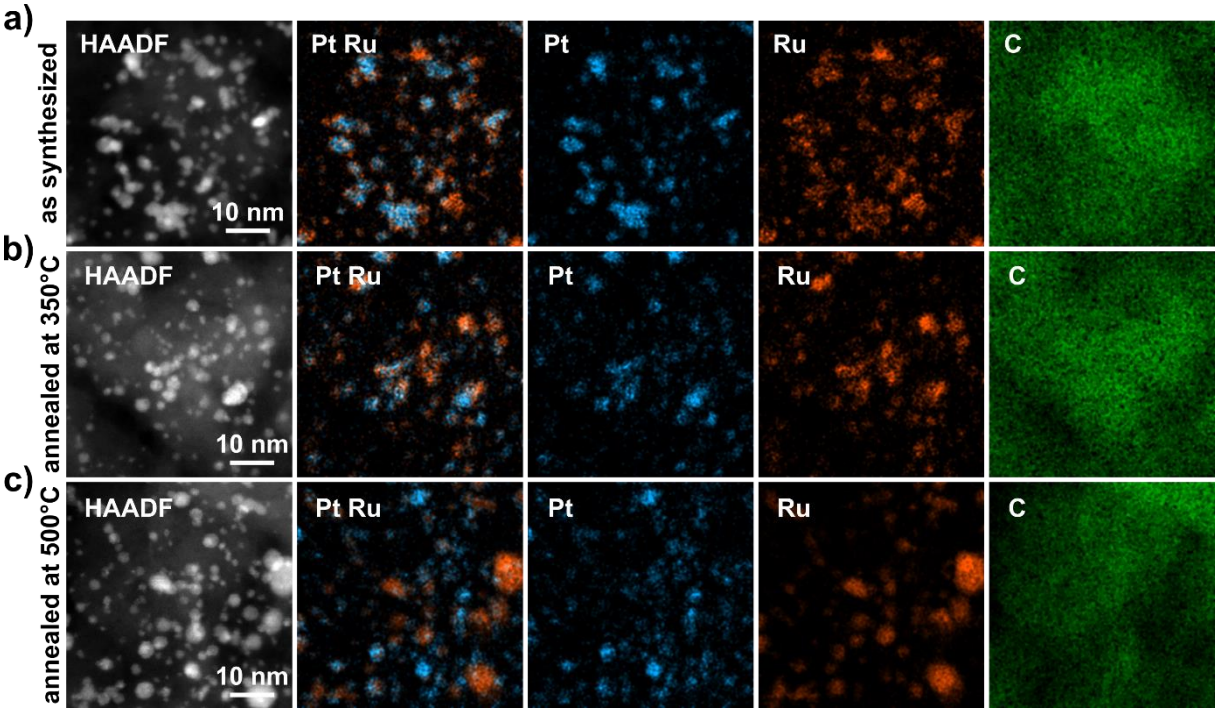

Figure 2: STEM-EDX spectrum images of a) $Ru_1@Pt_4/C$, b) Pt_4Ru_1/C-350, and c) Pt_4Ru_1/C-500. Pt in blue, Ru in orange, C in green.

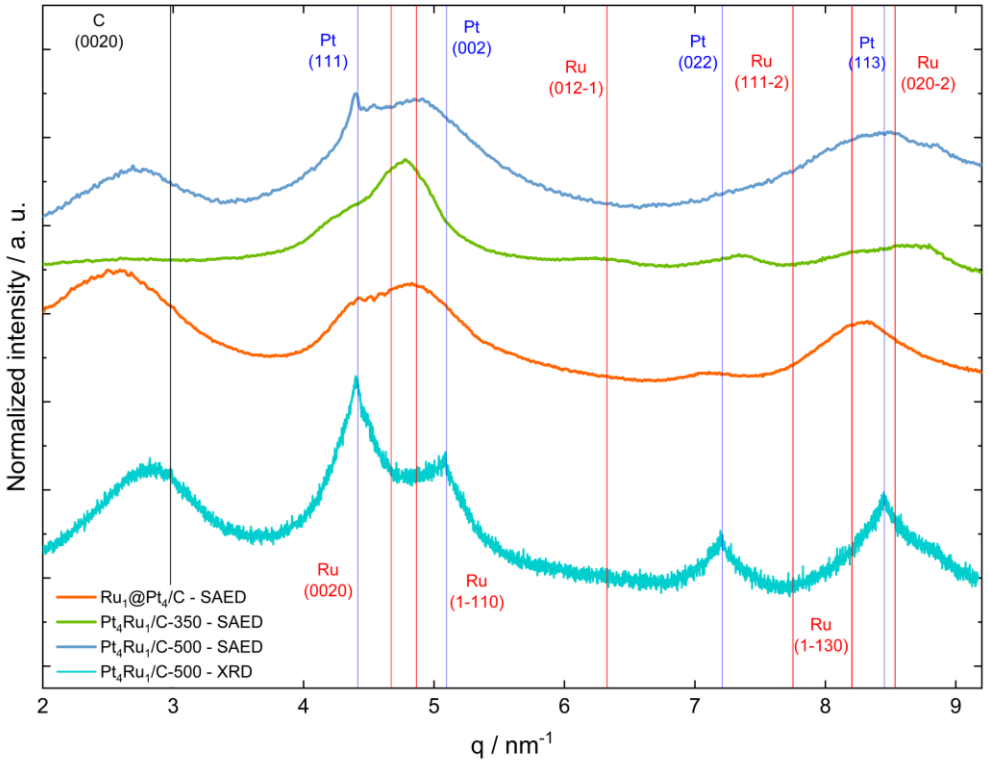

Figure 3: SAED analysis results of $Ru_1@Pt_4/C$ (red) and bimetallic Pt_4Ru_1/C catalysts (green, blue) and XRD pattern of Pt_4Ru_1/C-500 catalyst (turquoise) for comparison (Cu Kα radiation, λ = 1.542 Å).

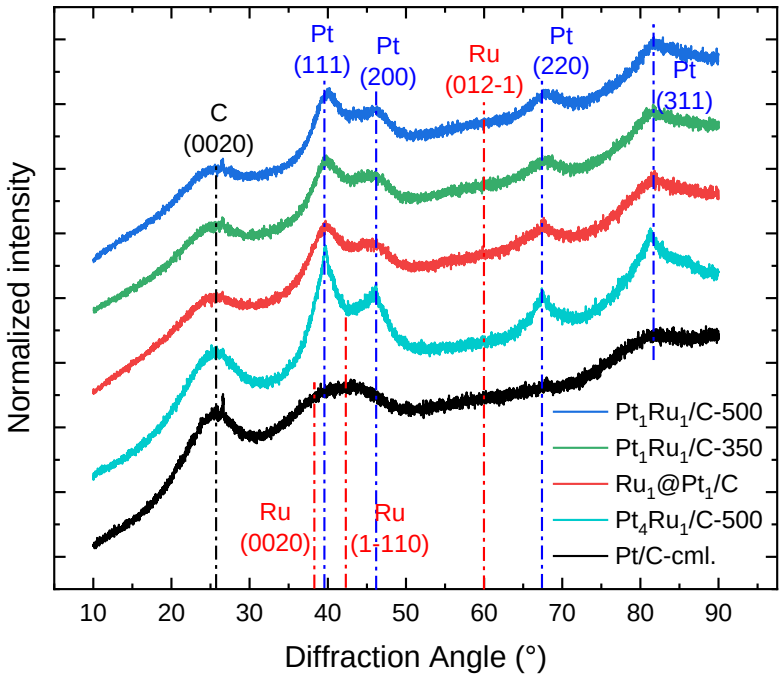

Figure 4: XRD patterns of pristine Pt/C (black), Pt_4Ru_1/C-500 (turquoise), $Ru_1@Pt_1/C$ (red) and bimetallic Pt_1Ru_1/C catalysts with different post-treatment temperatures (green, blue), Cu Kα radiation (λ = 1.542 Å).

To further clarify if there is an interaction between Pt und Ru in the bimetallic catalyst samples and to investigate the effect of thermal annealing on the composition of the metal particles, PDF analyses were conducted. In Figure 5 the results are compared for the $Ru_1@Pt_1/C$ (red) and the Pt_1Ru_1/C-500 (blue) sample. For better comparison, the residual (black) is shown in addition to the respective sample curves.

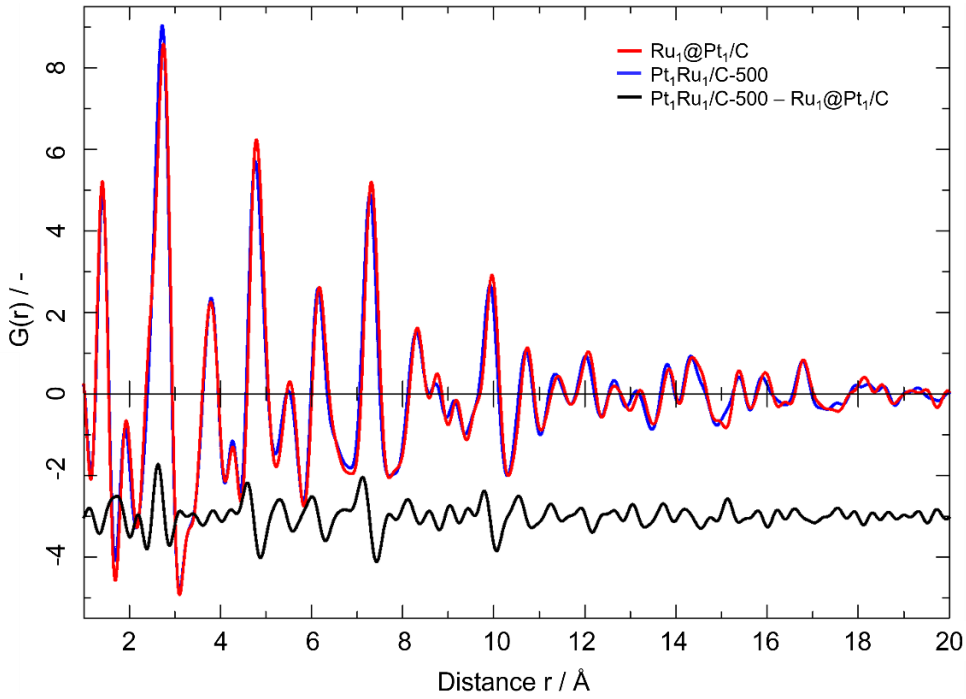

Figure 5: Comparison of PDF data of $Ru_1@Pt_1/C$ (red) and Pt_1Ru_1/C-500 (blue).

A remarkable observation is that all metal associated peaks shift to smaller lattice spacings after thermal annealing at 500 °C. This indicates that Ru atoms are incorporated into the Pt lattice causing a lattice contraction which agrees with the results of the XRD measurements (see Figure 4). Whereas Pt has a fcc crystal structure with a lattice constant of 3.92 Å[42], Ru forms hexagonal close-packed (hcp) crystals. Up to a Ru content of 0.7 mol%, Ru can form alloys with Pt, replacing Pt atoms but keeping the crystal structure intact. The lattice constant decreases down to a value of 3.83 Å[42] at a Ru content of 0.68%.[42,43] Moreover, Vegard's law states that the lattice parameters of a bimetallic particle/alloy lie between those of the two pure metals.[44] The expected lattice parameter for fcc ruthenium particles based on DFT simulation is 3.73 Å.[45] This agrees with our results of the PDF analyses and again leads to the conclusion that there is an interaction between Pt and Ru atoms. Thereby an elevated annealing temperature promotes the diffusion of Ru into the Pt nanoparticles of the catalyst.

Dehydrogenation of H14-BP

To evaluate the influence of Ru addition and different compositions of Pt_xRu_1 (x = 1, 2, 4, 8, and 16) on the activity and selectivity of Pt_xRu_1/C catalysts, the synthesized materials were tested in the dehydrogenation of H14-BP. A commercial Pt/C catalyst (Pt/C-cml.) from previous work by Zakegym *et al.*[11] was used as a benchmark. Additionally, a Pt/C catalyst that was subjected to our specific synthesis conditions without the addition of $RuCl_3$ (Pt/C-control) and a commercial Ru/C catalyst (Ru/C-cml.) were also tested for control purposes. The measured hydrogen release for the different reference and control catalysts over the reaction time is depicted in Figure 6.

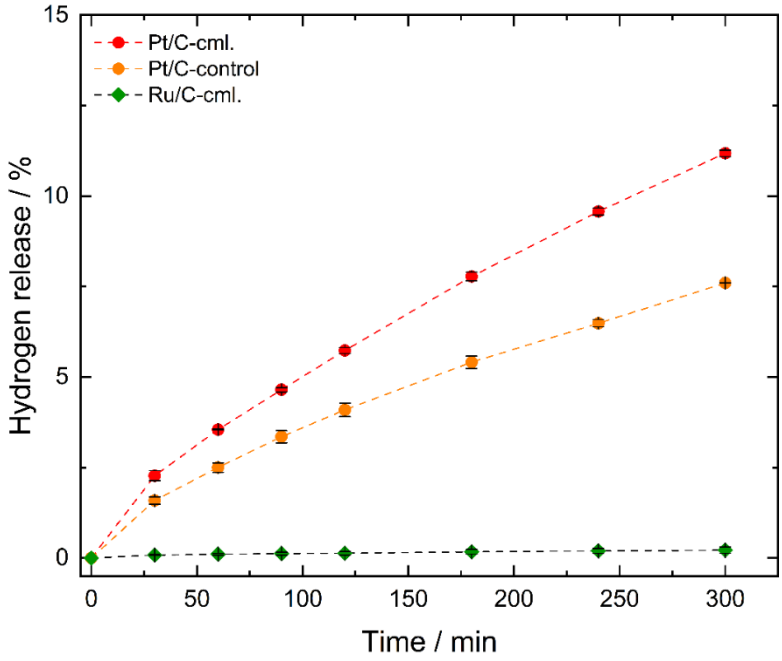

Figure 6: Hydrogen release over reaction time in the dehydrogenation of H14-BP with reference and control catalysts. Experimental conditions: 230 °C; 1 atm; 200 ml min^{-1} Ar; 0.05 mol% (Pt+Ru):H14-BP; standard deviation derived from two reproductions.

For the Pt/C-control catalyst that was subjected to the synthesis conditions without Ru addition, a 32% decrease in hydrogen release could be observed after the reaction time of 5 h compared to the untreated commercial reference material. This might be due to changes on the nanoparticle or support surface caused by the control treatment. An increase in activity due to the catalyst treatment during the synthesis can therefore be ruled out for all further experiments. The commercial Ru/C catalyst released only 0.22% of the stored hydrogen over a period of 5 h. This confirms the previous results by Zakgeym[46] and shows that a monometallic Ru catalyst exhibits negligible activity for the dehydrogenation of H14-BP.

Initially and to evaluate the influence of Ru in bimetallic catalysts, Pt_1Ru_1/C catalysts were prepared, post-treated at different temperatures, and tested in the dehydrogenation of H14-BP. The measured hydrogen release is compared with those of the monometallic Pt/C references in Figure 7.

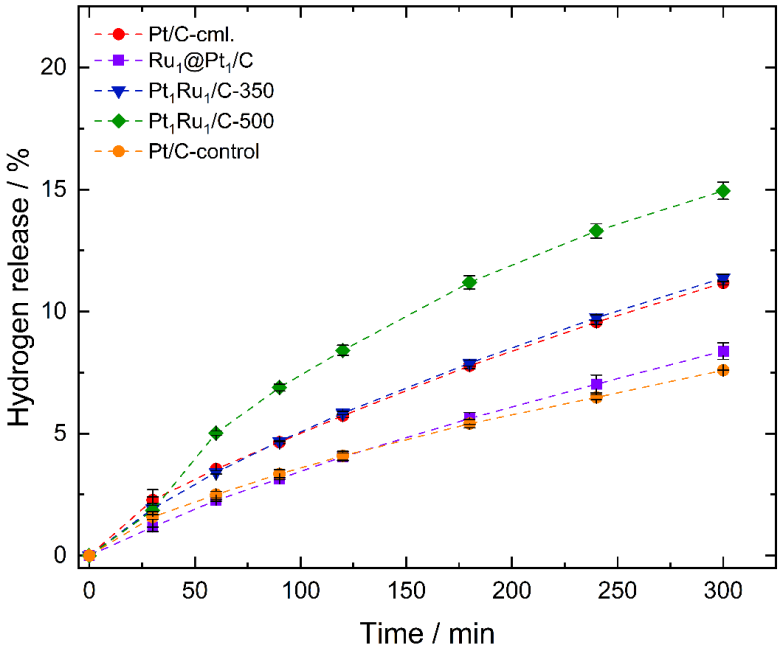

Figure 7: Hydrogen release of the Pt_1Ru_1/C catalysts over reaction time in the dehydrogenation of H14-BP with reference and control catalysts. Experimental conditions: 230 °C; 1 atm; 200 ml min^{-1} Ar; 0.05 mol% (Pt+Ru):H14-BP; standard deviation derived from two reproductions.

The Pt_1Ru_1 pre-catalyst without thermal post-treatment (Ru_1@Pt_1/C) shows a 31% decrease in hydrogen release compared to the Pt reference catalyst. With this, the achieved hydrogen release lies in the region of the Pt/C-control sample. But since the bimetallic catalysts contain more noble metal than the monometallic catalysts, the amount of catalyst used for the experiments was adjusted to maintain a constant ratio of LOHC to noble metal. As a result, 50% less Pt is available for the reaction in the experiments with Pt_1Ru_1/C compared to the standard experiment. This means that the platinum-based productivity is even higher for the bimetallic catalysts than for the monometallic ones. Nevertheless, the low activity of the Ru_1@Pt_1/C can be attributed to the fact that Ru is deposited onto the surface of the Pt particles during the synthesis. Without annealing, no diffusion of Ru into the Pt particles takes place. As a result, Ru covers the catalytically active surface of the Pt nanoparticles. Part of the active Pt surface is thus not available for the catalysis of the dehydrogenation reaction.

The Pt_1Ru_1/C catalyst post-treated at 350 °C shows a significant increase in activity compared to the one without thermal post-treatment. This can be attributed to the diffusion of Ru into

platinum particles. As a result, more active platinum surface area is available for the reaction than without thermal post-treatment. Despite providing only half of the total platinum amount, the catalyst showed comparable activity to the untreated standard catalyst with a hydrogen release of 11% after 5 h. This behavior suggests a synergistic effect between Pt and Ru. A possible explanation is that the diffusion of ruthenium into the noble metal particles modifies the chemical and geometrical properties of the surface.[13,47]

The Pt_1Ru_1/C-500 catalyst shows the highest hydrogen release rate in this series of experiments. The achieved hydrogen release of 15% after 5 h corresponds to a 31% increase in comparison to the standard catalyst. By increasing the post-treatment temperature, more ruthenium diffuses into the Pt particles and more Pt is present at the catalyst surface. The phase diagram of Pt and Ru (Figure S6) shows that the two metals are not completely miscible over a wide range of compositions.[48] At an atomic ratio Pt:Ru of 1:1, two phases are formed: a pure Pt phase and an alloy with the highest possible Pt concentration of 60%. The STEM-EDX spectrum images suggest that this occurs in the form of platinum nanoclusters on the surface of the bimetallic nanoparticles (c.f. Figure 2).

The formation of such nanoclusters and segregation phenomena have already been described in other works[49,50]. Sachse *et al.*[49] studied Pt-Ru nanoparticles on carbon films. They observed the formation of Pt nanoclusters on the surface of the nanoparticles during the reduction of the metals. Bavand *et al.*[50] described that there are no significant diffusion or changes in nanoparticle composition during thermal annealing of Pt-Ru at temperatures below 250 °C. Between 250 and 350 °C, rapid diffusion was observed. In another study[42] on Pt-Ru nanoparticles prepared by chemical reduction, no alloy formation was found below 350 °C. This is in good agreement with our results. Without thermal annealing at 350 °C, no positive effects due to the presence of Ru on the catalyst surface and the absence of Pt-Ru interactions were observed.[42]

In this context, a change in the electronic structure of Pt atoms at the particle surface through neighboring Ru atoms is possible. Fine-tuning the electronic properties of platinum has proven to be a valuable tool for increasing catalyst activity[51,52]. For example, *Chen et. al*.[52] were able to increase the activity of Pt nanoparticles for ammonia borane hydrolysis by a factor of 15 by specifically adjusting their ionic structure. In comparison to single-metal configurations, bimetallic systems often feature distinct electronic characteristics that can be advantageous for fine-tuning the adsorbate-catalyst surface interactions.[53] This can reduce, for example, the

adsorption energy of hydrogen at the active sites[49] which can have again a positive impact on the dehydrogenation activity. DFT simulations[54] showed that the interaction of the different atoms in a nanostructure can lead to so-called ligand effects. The incorporation of a heteroatom into a metallic particle leads to a broadening or narrowing of the d-band and a corresponding change in the average d-band energy. This change in the electronic structure leads to a change in the chemical properties of the surface atoms. Studies on model Ru surfaces showed that a shift in the mean energy of the d-band causes a stronger interaction with adsorbates. In contrast, lowering the mean d-band energy weakens the interaction between adsorbate and surface.[44]

Based on the explanations above, the increased catalytic activity of the bimetallic Pt_1Ru_1 nanoparticles was attributed to the formation of platinum nanoclusters and an interaction between Pt and Ru, which results in altered adsorption properties.

To further study the role of Ru in the bimetallic catalysts and determine the optimum amount of Ru, catalysts with Pt:Ru ratios of 2:1, 4:1, 8:1, and 16:1 were synthesized and tested in the dehydrogenation of H14-BP. In Figure 8, the overall hydrogen release in the dehydrogenation experiments is compared for the different catalysts.

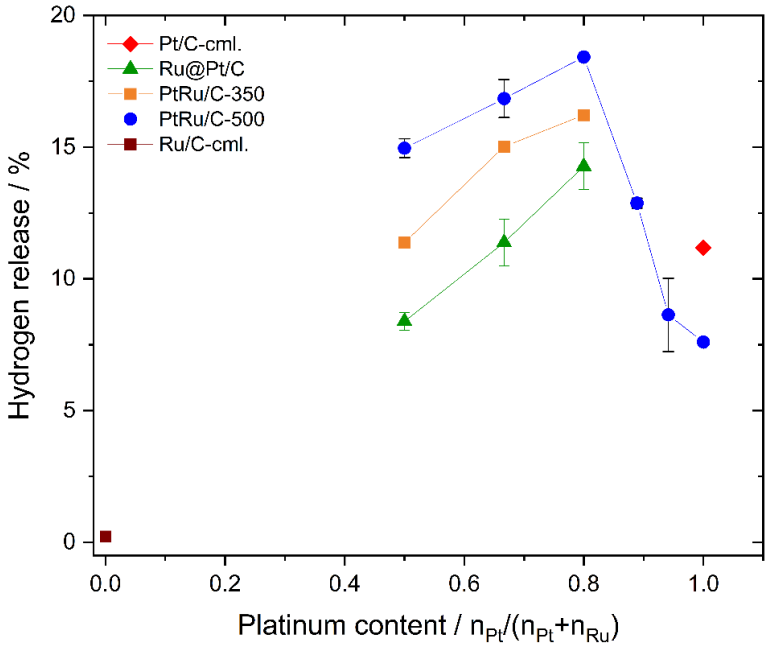

Figure 8: Hydrogen released after 5 h reaction time in the dehydrogenation of H14-BP over the platinum content of the metal particles with reference and control catalysts. Experimental conditions: 230 °C; 1 atm; 200 ml min^{-1} Ar; 0.05 mol% (Pt+Ru):H14-BP; standard deviation derived from two reproductions.

The correlation between a higher post-treatment temperature and an increased catalyst activity was, once again, confirmed for Pt:Ru molar ratios of 1:1, 2:1 and 4:1. Hence, the catalysts with Pt:Ru ratios of 8:1 and 16:1 were exclusively annealed at 500 °C. Starting from a Pt:Ru ratio of

1:1, the overall hydrogen release increases with decreasing Ru content in the catalyst. A maximum is observed at a Pt:Ru ratio of 4:1. Thereafter, a sharp decrease of hydrogen release after is (or can be?) observed for higher ratios. Interestingly and contrary to $Ru_1@Pt_1/C$, even the $Ru_1@Pt_4/C$ catalyst shows a higher activity than the standard catalyst. The measured hydrogen release during the experiment amounts to 14% and is therefore 28% higher than the one exhibited by the reference.

Due to the constant LOHC to noble metal ratio of 2000:1, more Pt is available for the reaction when using Pt_4Ru_1 catalysts than when using Pt_1Ru_1 catalysts. Consequently, the amount of Ru in the untreated $Ru_1@Pt_4/C$ catalyst cannot cover the complete surface of the Pt nanoparticles. This leads to two effects: 1) A part of Pt atoms remains at the particle surface and is still active for the reaction. 2) A Pt-Ru interface, that would only be formed through thermal annealing for a completely Ru covered surface, is already present without post-treatment. Like in Pt_1Ru_1/C-500, this PtRu surface is then particularly active for the dehydrogenation of H14-BP.

For a more detailed consideration of the most active catalyst Pt_4Ru_1/C-500, the hydrogen release and the productivity curves are shown together with the reference curves of the Pt/C-cml. catalyst in Figure 9.

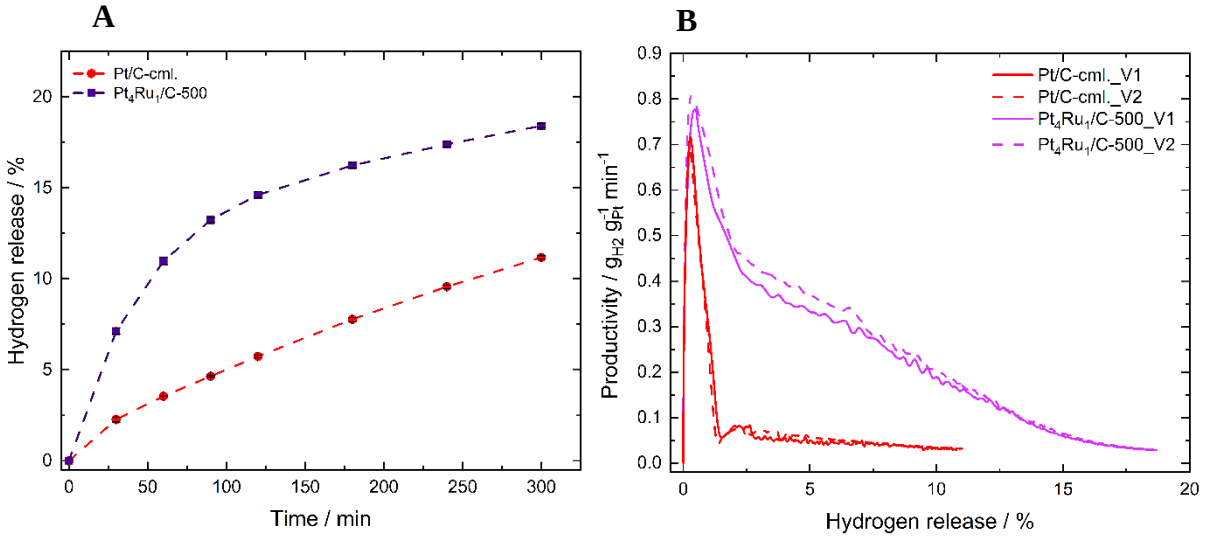

Figure 9: Hydrogen release over reaction time (A) and productivity over hydrogen release (B) of the Pt_4Ru_1/C catalysts in the dehydrogenation of H14-BP with reference catalysts. Experimental conditions: 230 °C; 1 atm; 200 ml min^{-1} Ar; 0.05 mol% (Pt+Ru):H14-BP; standard deviation derived from two reproductions.

The comparison of the hydrogen release of the Pt_4Ru_1/C-500 catalyst with the standard sample (Figure 9, A) confirms the higher activity of the Ru-containing catalyst. The achieved hydrogen release of 18% after 5 h reaction time corresponds to an increase of 65% compared to the pure Pt catalyst. This was determined from the composition of the liquid samples at the end of the

experiment (see Table S5). It can be further seen from the liquid phase compositions that with the Pt_4Ru_1/C-500 catalyst nearly complete H14-BP conversion (98%) was achieved, mostly resulting in ketone formation (74%) but also partly in dehydration and further ring dehydrogenation (24%). The H14-BP conversion with the Pt/C in contrast only amounted to 55% which is made up to 31% of ketone formation and to 13% of consequential reactions.

The observed activity increase with the addition of Ru to the Pt/C catalyst (molar ratio 1:4) is attributed to the formation of a PtRu nanostructure as described above. Ru thereby affects the formation of Pt nanoclusters on the nanoparticle surface. More of these Pt nanoclusters are assumed to be formed at a higher proportion of Pt in the catalyst, which results in an increased activity. In this regard, the Pt:Ru ratio of 4:1 appears to provide the optimum proportion of Pt nanoclusters and therefore the highest activity of the corresponding catalysts. The high annealing temperature of 500 °C again contributes to a successful formation of the active Pt nanoclusters.

To exclude the influence of different platinum contents, the productivity of the Pt_4Ru_1/C-500 and the standard catalysts are calculated in relation to the Pt mass (Figure 9, B). The productivity of the untreated standard catalyst shows a sharp productivity maximum at the beginning of the experiment. The maximum productivity of 0.72 $g_{H2}\, g_{Pt}\, min^{-1}$ thereby is comparable with the one of the Pt_4Ru_1/C-500 catalyst. However, the productivity of the standard catalyst drops shortly after reaching the maximum value. In contrast, the productivity of the Ru-containing catalyst remains on a higher level over a wider range of the degree of hydrogen release. This results in an overall higher productivity of the bimetallic catalyst. The slower drop in productivity of the PtRu catalysts compared to the pure Pt catalyst fits the described changes in the adsorption properties of the bimetallic catalysts. Lowering the average d-band energy facilitates the desorption of the products. This allows the bimetallic catalysts to maintain a high productivity over a wider range of hydrogen release than the monometallic Pt catalyst.

Conclusion

In this contribution, the use of bimetallic PtRu/C catalysts for the dehydrogenation of H14-BP was investigated. The catalysts were synthesized by deposition of Ru onto a Pt/C reference material, followed by thermal annealing. A significant increase in hydrogen release was observed for the Ru containing catalysts. A monometallic Ru/C catalyst showed no activity for the dehydrogenation reaction. Different Pt:Ru ratios of 1:1, 2:1, 4:1, 8:1, and 16:1 were investigated and compared with the pristine and control catalysts. The highest activities were achieved with the ratio of 4:1. In addition, the effect of the thermal annealing temperature on the structure of the catalyst and its dehydrogenation activity was investigated. Overall, an increasing activity with increasing annealing temperature was found. The highest hydrogen release within this study was achieved by a bimetallic catalyst with a Ru content of 20% and an annealing temperature of 500 °C. This corresponds to an increase in hydrogen release of 65% in comparison to the standard Pt/C catalyst.

Diffusion of Ru into the catalyst nanoparticles through thermal annealing was shown. XRD and PDF measurements suggest the incorporation of Ru into the fcc crystal structure of the Pt nanoparticles and the presence of an interaction between the two metals. For the considered Pt:Ru ratios, partial segregation, and the formation of Pt nanoclusters on the surface of the bimetallic particles is assumed. This is supported by STEM-EDXS measurements.

The formation of Pt nanoclusters on the surface of the nanoparticles is associated with a high Pt dispersion. This contributes to an increased dehydrogenation activity of the corresponding catalysts. Moreover, the incorporation of Ru into the Pt nanoparticles is assumed to have an electronic effect: Through a broadening of the d-band and a decrease in its average energy, the adsorption energy of a molecule on the surface of the bimetallic particle is reduced, leading to a facilitated desorption of reaction products. This is reflected in the behavior of the most active catalyst Pt_4Ru_1/C-500. A higher maximum productivity compared to the reference Pt catalyst is achieved. Further, the productivity remains on a higher level over a longer range of the degree of hydrogen release. Both effects are attributed to a favorable composition of the bimetallic catalyst nanoparticles with a high share of Pt nanoclusters and favorable adsorption properties.

The applied synthesis procedure to post-treat a commercial Pt/C catalyst with Ru and yield alloyed metal structures with altered surface properties could be also relevant for other types of

catalytic reactions. Moreover, the procedure could be transferred regarding other catalyst materials and metal alloys.

Author contributions

LM: conceptualization; investigation, data curation & formal analysis (catalyst testing, XRD); formal analysis (HAADF-STEM); visualization; writing – original draft. **CP**: conceptualization; investigation, data curation & formal analysis (catalyst preparation & activation, XRD, STEM-EDX); visualization; writing – original draft. **BF**: formal analysis (SAED); writing – review & editing. **HJ**: investigation (SPXRD). **ME**: resources and supervision (SPXRD); data curation & formal analysis (SPXRD); writing – review & editing. **AH**: investigation & formal analysis (HAADF-STEM, STEM-EDX); visualization; supervision (HAADF-STEM, STEM-EDX, SAED); writing – review & editing. **RN**: investigation, data curation & formal analysis (PDF); visualization (PDF); writing – review & editing. **MW**: conceptualization; project administration; supervision; writing – review & editing. **FA**: conceptualization; visualization; validation; project administration; supervision; writing – original draft. **ST**: conceptualization; funding acquisition; project administration; resources; writing – review & editing. **PW**: conceptualization; funding acquisition; project administration; resources; writing – review & editing.

Conflicts of interest

Peter Wasserscheid is founder and minority shareholder of the company Hydrogenious LOHC technologies (www.hydrogenious.net) that offers commercially hydrogen storage systems based on the LOHC technology. There is no conflict of interest to declare about the specific scientific results reported in this paper.

Acknowledgements

This work was funded by the Bavarian Ministry of Economic Affairs, Regional Development and Energy through the project “Emissionsfreier und stark emissionsreduzierter Bahnverkehr auf nicht-elektrifizierten Strecken” and by the Helmholtz Research Program “Materials and Technologies for the Energy Transition (MTET), Topic 3: Chemical Energy Carriers”. We acknowledge DESY (Hamburg, Germany), a member of the Helmholtz Association HGF, for

the provision of experimental facilities. Parts of this research were carried out at PETRA III beamline P02.1. Beamtime was allocated by an in-house contingent. Additional thanks go to Elisabeth Herzinger and Armin Lautenbach for the conduction of the ICP-OES measurements. The authors would also like to thank Dr. Jonas Hofmann for hydrogenation experiments to provide the educt H14-BP and Dr. Andreas Bösmann for fruitful discussions.

Table of contents

Bimetallic PtRu/C catalysts were prepared by an innovative synthesis method. Various characterization techniques were applied to show that diffusion of Ru into the crystal structure of the Pt nanoparticles takes place during thermal annealing. The most active bimetallic catalyst exhibited a 65% increase in hydrogen release productivity during the catalytic dehydrogenation of the LOHC compound dicyclohexylmethanol compared to monometallic Pt/C.

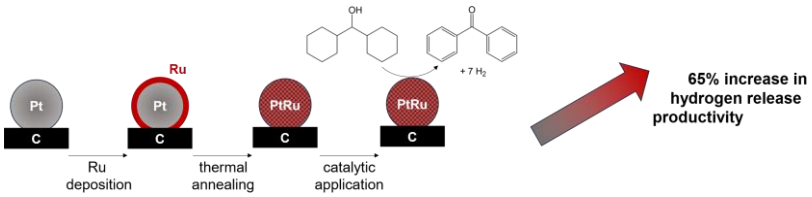

References

[1] P. Preuster, C. Papp, P. Wasserscheid, *Accounts of chemical research* **2017**, *50*, 74.

[2] M. H. Hamayun, I. M. Maafa, M. Hussain, R. Aslam, *Energies* **2020**, *13*, 206.

[3] M. R. Usman, D. L. Cresswell, *International Journal of Green Energy* **2013**, *10*, 177.

[4] N. Brückner, K. Obesser, A. Bösmann, D. Teichmann, W. Arlt, J. Dungs, P. Wasserscheid, *ChemSusChem* **2014**, *7*, 229.

[5] H. Jorschick, P. Preuster, S. Dürr, A. Seidel, K. Müller, A. Bösmann, P. Wasserscheid, *Energy Environ. Sci.* **2017**, *10*, 1652.

[6] H. Jorschick, S. Dürr, P. Preuster, A. Bösmann, P. Wasserscheid, *Energy Technol.* **2019**, *7*, 146.

[7] T. Rüde, S. Dürr, P. Preuster, M. Wolf, P. Wasserscheid, *Sustainable Energy Fuels* **2022**, *6*, 1541.

[8] K. Müller, T. Skeledzic, P. Wasserscheid, *Energy Fuels* **2021**, *35*, 10929.

[9] Z. Feng, X. Chen, X. Bai, *Environmental science and pollution research international* **2020**, *27*, 36172.

[10] K. Paragian, B. Li, M. Massino, S. Rangarajan, *Mol. Syst. Des. Eng.* **2020**, *5*, 1658.

[11] D. Zakgeym, J. D. Hofmann, L. A. Maurer, F. Auer, K. Müller, M. Wolf, P. Wasserscheid, *Sustainable Energy Fuels* **2023**, *7*, 1213.

[12] J. Da Han, Y. S. Jo, B. S. Shin, M. Jang, J. W. Kang, J. H. Han, S. W. Nam, C. W. Yoon, *Energy Technol.* **2019**, *7*, 113.

[13] W. Sachtler, R. A. van Santen, Vol. 26, Elsevier **1977**, p. 69.

[14] P. J. Kulesza, I. S. Pieta, I. A. Rutkowska, A. Wadas, D. Marks, K. Klak, L. Stobinski, J. A. Cox, *Electrochimica Acta* **2013**, *110*, 474.

[15] F. Vigier, C. Coutanceau, F. Hahn, E. M. Belgsir, C. Lamy, *Journal of Electroanalytical Chemistry* **2004**, *563*, 81.

[16] O. A. Petrii, *J Solid State Electrochem* **2008**, *12*, 609.

[17] J. E. Mueller, P. Krtil, L. A. Kibler, T. Jacob, *Physical chemistry chemical physics PCCP* **2014**, *16*, 15029.

[18] E. Liu, L. Jiao, J. Li, T. Stracensky, Q. Sun, S. Mukerjee, Q. Jia, *Energy Environ. Sci.* **2020**, *13*, 3064.

[19] E. R. Hamo, R. K. Singh, J. C. Douglin, S. Chen, M. B. Hassine, E. Carbo-Argibay, S. Lu, H. Wang, P. J. Ferreira, B. A. Rosen, D. R. Dekel, *ACS Catal.* **2021**, *11*, 932.

[20] Z. Zhang, J. Liu, J. Wang, Q. Wang, Y. Wang, K. Wang, Z. Wang, M. Gu, Z. Tang, J. Lim, T. Zhao, F. Ciucci, *Nature communications* **2021**, *12*, 5235.

[21] B. Jiang, C. Li, V. Malgras, M. Imura, S. Tominaka, Y. Yamauchi, *Chemical science* **2016**, *7*, 1575.

[22] W. Qiao, X. Huang, L. Feng, *Chinese Journal of Structural Chemistry* **2022**.

[23] Y. Bao, F. Wang, X. Gu, L. Feng, *Nanoscale* **2019**, *11*, 18866.

[24] Y.-L. Zhang, J.-L. Li, L. Zhao, X.-L. Sui, Q.-Y. Zhou, X.-F. Gong, J.-J. Cai, J.-Z. Li, D.-M. Gu, Z.-B. Wang, *Electrochimica Acta* **2020**, *331*, 135410.

[25] Jia Tang, Xiao-Ming Zhang, Shan-Sheng Yu, Su-Li Wang, and Gong-Quan Sun.

[26] M. Xiao, L. Feng, J. Zhu, C. Liu, W. Xing, *Nanoscale* **2015**, *7*, 9467.

[27] M. Minichová, C. van Pham, B. Xiao, A. Savan, A. Hutzler, A. Körner, I. Khalakhan, M. G. Rodríguez, I. Mangoufis-Giasin, V. Briega-Martos, A. Kormányos, I. Katsounaros, K. J. Mayrhofer, A. Ludwig, S. Thiele, S. Cherevko, *Electrochimica Acta* **2023**, *444*, 142032.

[28] B. Fritsch, M. Wu, A. Hutzler, D. Zhou, R. Spruit, L. Vogl, J. Will, H. Hugo Pérez Garza, M. März, M. P. M. Jank, E. Spiecker, *Ultramicroscopy* **2022**, *235*, 113494.

[29] F. Niekiel, S. M. Kraschewski, J. Müller, B. Butz, E. Spiecker, *Ultramicroscopy* **2017**, *176*, 161.

[30] J. Filik, A. W. Ashton, P. C. Y. Chang, P. A. Chater, S. J. Day, M. Drakopoulos, M. W. Gerring, M. L. Hart, O. V. Magdysyuk, S. Michalik, A. Smith, C. C. Tang, N. J. Terrill, M. T. Wharmby, H. Wilhelm, *Journal of applied crystallography* **2017**, *50*, 959.

[31] S. J. L. Billinge, C. L. Farrow, *Journal of physics. Condensed matter an Institute of Physics journal* **2013**, *25*, 454202.

[32] P. Juhás, T. Davis, C. L. Farrow, S. J. L. Billinge, *Journal of applied crystallography* **2013**, *46*, 560.

[33] T. Proffen, R. B. Neder, *Journal of applied crystallography* **1999**, *32*, 838.

[34] None Available, *Materials Data on Pt by Materials Project*, LBNL Materials Project; Lawrence Berkeley National Laboratory (LBNL), Berkeley, CA (United States) **2020**.

[35] W. H. Lizcano-Valbuena, V. A. Paganin, E. R. Gonzalez, *Electrochimica Acta* **2002**, *47*, 3715.

[36] J. C. M. Silva, S. Ntais, V. Rajaraman, É. Teixeira-Neto, Â. A. Teixeira-Neto, A. O. Neto, R. M. Antoniassi, E. V. Spinacé, E. A. Baranova, *Electrocatalysis* **2019**, *10*, 203.

[37] E. Lust, E. Härk, J. Nerut, K. Vaarmets, *Electrochimica Acta* **2013**, *101*, 130.

[38] G. Álvarez, F. Alcaide, O. Miguel, L. Calvillo, M. J. Lázaro, J. J. Quintana, J. C. Calderón, E. Pastor, *J Solid State Electrochem* **2010**, *14*, 1027.
[39] D. Chu, S. Gilman, *J. Electrochem. Soc.* **1996**, *143*, 1685.
[40] P. Scherrer, *Nachrichten von der Gesellschaft der Wissenschaften zu Göttingen, Mathematisch-Physikalische Klasse* **1918**, *1918*, 98.
[41] G. Bergeret, P. Gallezot.
[42] E. Antolini, F. Cardellini, *Journal of Alloys and Compounds* **2001**, *315*, 118.
[43] E. Raub, *Journal of the Less Common Metals* **1959**, *1*, 3.
[44] M. Luo, S. Guo, *Nat Rev Mater* **2017**, *2*.
[45] Y. Yao, in *Controllable Synthesis and Atomic Scale Regulation of Noble Metal Catalysts* (Ed.: Y. Yao), Springer Singapore. Singapore **2022**, p. 33.
[46] D. Zakgeym, *Katalysator- und Prozessentwicklung für sauerstoffhaltige flüssige organische Wasserstoffträger-Systeme* **2022**.
[47] K. Ding (Ed.), *Handbook of asymmetric heterogeneous catalysis*, Wiley-VCH Verl., Weinheim **2008**.
[48] H. Okamoto, *J Phs Eqil and Diff* **2008**, *29*, 471.
[49] R. Sachse, D. Bernsmeier, R. Schmack, I. Häusler, A. Hertwig, K. Kraffert, J. Nissen, R. Kraehnert, *Catal. Sci. Technol.* **2020**, *10*, 2057.
[50] R. Bavand, A. Korinek, G. A. Botton, A. Yelon, E. Sacher, *J. Phys. Chem. C* **2017**, *121*, 23104.
[51] W. Chen, G. Qian, Y. Wan, de Chen, X. Zhou, W. Yuan, X. Duan, *Accounts of chemical research* **2022**, *55*, 3230.
[52] W. Chen, W. Fu, X. Duan, B. Chen, G. Qian, R. Si, X. Zhou, W. Yuan, de Chen, *Engineering* **2022**, *14*, 124.
[53] X. Zhang, X. Xiao, J. Chen, Y. Liu, H. Pan, W. Sun, M. Gao, *Energy Environ. Sci.* **2022**, *15*, 4511.
[54] J. R. Kitchin, J. K. Nørskov, M. A. Barteau, J. G. Chen, *Physical review letters* **2004**, *93*, 156801.

Additional references are used and cited in the Supporting Information.

[S1] H. Okamoto, *J. Phs. Eqil. and Diff.* **2008**, 29, 471.